High-speed atomic force microscopy reveals structural dynamics of amyloid β_{1-42} aggregates

Takahiro Watanabe-Nakayama[a,1], Kenjiro Ono[b,c,1], Masahiro Itami[a], Ryoichi Takahashi[b], David B. Teplow[d], and Masahito Yamada[b,2]

[a]Bio-AFM Frontier Research Center, Kanazawa University, Kanazawa 920-1192, Japan; [b]Department of Neurology and Neurobiology and Aging, Kanazawa University Graduate School of Medical Sciences, Kanazawa 920-8640, Japan; [c]Department of Neurology, Showa University School of Medicine, Tokyo 142-8666, Japan; and [d]Department of Neurology, The University of California, Los Angeles School of Medicine, Los Angeles, CA 90095

Edited by G. Marius Clore, National Institutes of Health, Bethesda, MD, and approved April 11, 2016 (received for review December 19, 2015)

Aggregation of amyloidogenic proteins into insoluble amyloid fibrils is implicated in various neurodegenerative diseases. This process involves protein assembly into oligomeric intermediates and fibrils with highly polymorphic molecular structures. These structural differences may be responsible for different disease presentations. For this reason, elucidation of the structural features and assembly kinetics of amyloidogenic proteins has been an area of intense study. We report here the results of high-speed atomic force microscopy (HS-AFM) studies of fibril formation and elongation by the 42-residue form of the amyloid β-protein ($A\beta_{1-42}$), a key pathogenetic agent of Alzheimer's disease. Our data demonstrate two different growth modes of $A\beta_{1-42}$, one producing straight fibrils and the other producing spiral fibrils. Each mode depends on initial fibril nucleus structure, but switching from one growth mode to another was occasionally observed, suggesting that fibril end structure fluctuated between the two growth modes. This switching phenomenon was affected by buffer salt composition. Our findings indicate that polymorphism in fibril structure can occur after fibril nucleation and is affected by relatively modest changes in environmental conditions.

Alzheimer's disease | amyloidogenic proteins | kinetics | atomic force microscopy

Amyloid fibril accumulation is associated with numerous neurodegenerative diseases, including Alzheimer's (AD) (1–3), prionoses (4–7), Parkinson's (8–11), and Huntington's (12). Nonhomologous genes encode the proteins involved in each disease, namely the amyloid β-protein (Aβ), prions (e.g., PrP, Sup35, Het-s), α-synuclein, and huntingtin, respectively. Each of these proteins assembles from a monomer state through a variety of intermediates to form insoluble amyloid fibrils that accumulate in brain tissues. The suggestion that brain Aβ accumulation and neurodegeneration are correlated remains an area of contention. Studies of human brain extracts and transgenic mice suggest such a correlation does not exist (13, 14), whereas other studies support this relationship (15). Amyloid deposition in the brain does correlate with progress from mild cognitive impairment to AD (16). The amount of brain amyloid in asymptomatic elderly people generally is less than in AD patients (17). Historically, amyloid fibrils have been regarded as the key pathologic agents in AD. This idea has been supplanted by theories in which oligomers are central (18, 19). A variety of studies support this view (20–23). In addition, oligomers appear to be more toxic to cultured cells than are fibrils (24, 25). Nevertheless, Aβ40 fibrils are neurotoxic (24, 26–28) and fibrillar Aβ appears to be associated with inflammation (29, 30) and oxidative damage (31, 32) in the brain. We believe that an unbiased assessment of working theories of disease causation does not allow one to conclude that the two theories are mutually exclusive. It is more likely that both types of assemblies are involved in AD pathogenesis. In fact, Lu et al. have provided support for this more inclusive theory by arguing that oligomers and fibrils exist in equilibrium (33). Such an equilibrium is thought to include, in addition, monomers and protofibrils (34).

Although specific intermediates and fibrils have been studied in isolation at particular stages of Aβ assembly, it has been more difficult to observe structural transitions that may occur among assembly types. Techniques such as thioflavin-T (ThT) fluorescence, circular dichroism spectroscopy, and Fourier transform infrared spectroscopy are widely used to monitor development of β-sheet structure, but these methods do not provide information on aggregate tertiary or quaternary structure. Structural studies using X-ray crystallography or solid-state NMR have provided useful information on protein structure at the atomic level, but this information is static in nature and does not reveal aspects of the gross structural transitions among assembly states. Electron microscopy also is a static method.

The process of fibril formation itself has been shown to be more complicated than originally thought. One reason is the huge conformational space of the intrinsically disordered Aβ monomer, which gives rise to many different oligomer structures, some of which are on-pathway for fibril formation and some of which are not. This diversity of prefibrillar structures is reflected in the structures of the fibrils that then form. Fibrils are polymorphic—Aβ forms fibrils with distinct structures depending on experimental conditions (35, 36). Additionally, different fibril types have different impacts on neurodegeneration (26, 33, 37–39). Thus, characterization of the structural dynamics of the fibril formation process is an important endeavor. Real-time visualization of monomer aggregation and fibril formation offers the possibility of understanding the dynamics of the system, developing hypotheses about assembly mechanisms, and elucidating aggregation mechanisms.

Significance

Amyloid fibril formation underlies the pathogenesis of a large number of diseases. Among the neurodegenerative diseases, the process is prominent in Alzheimer's disease. Fibril elongation has been thought to be a nucleation-dependent process that faithfully duplicates nucleus structure as each monomer adds to the fibril end. Polymorphism in fibril structure thus has been postulated to depend on initial nucleus structure. However, there is little direct observation of growing amyloid fibril structure. Here, using high-speed atomic force microscopy, we observed that $A\beta_{1-42}$ fibril formation produced two distinct morphomers, "straight" and "spiral." Surprisingly, we observed switching between these structures after the initiation of fibril elongation. Our results provide previously unidentified insights into the process of nucleation-dependent $A\beta_{1-42}$ fibril formation.

Author contributions: T.W.-N., K.O., and M.Y. designed research; T.W.-N., K.O., M.I., R.T., and M.Y. performed research; T.W.-N. contributed new reagents/analytic tools; T.W.-N., K.O., D.B.T., and M.Y. analyzed data; and T.W.-N., K.O., D.B.T., and M.Y. wrote the paper.

The authors declare no conflict of interest.

This article is a PNAS Direct Submission.

[1]T.W.-N. and K.O. contributed equally to this work.

[2]To whom correspondence should be addressed. Email: m-yamada@med.kanazawa-u.ac.jp.

This article contains supporting information online at www.pnas.org/lookup/suppl/doi:10.1073/pnas.1524807113/-/DCSupplemental.

In the present study, we used high-speed atomic force microscopy (HS-AFM) (40, 41) to study the dynamics of $A\beta_{1–42}$ assembly. We were able to visualize initial fibril nucleation and subsequent fibril elongation. We observed two distinct growth modes for $A\beta_{1–42}$ fibrils—one producing straight fibrils and one producing spiral fibrils—and, unexpectedly, morphological switching between these two modes.

Results

HS-AFM Imaging of Temporal Changes in Low- and High-Molecular-Weight $A\beta_{1–42}$ Fractions. In preparation for HS-AFM observation, we separated $A\beta_{1–42}$ peptides into low- and high-molecular-weight populations (LMW and HMW, respectively) and confirmed that their structure and assembly properties were consistent with previous studies (*Supporting Information* and Figs. S1 and S2) (28, 42–49). The LMW population comprised monomeric and low-order oligomeric $A\beta_{1–42}$ (28). The HMW population contained higher-order oligomers (Fig. S1).

We then used HS-AFM to monitor the assembly of LMW (Fig. 1) and HMW (Fig. S3). Time 0 corresponds to the time when 100 mM NaCl was added to accelerate the assembly process. We observed nonfibrous particles with LMW initially (~1,800 s), as shown in Fig. 1*B* (Movie S1). Subsequently, objects with fibrillar morphologies began to accumulate. These objects elongated during observation. Assembly height fluctuated between ~5 and 10 nm with a periodicity of ~100 nm, corresponding to a spiral structure (Fig. 1 *B* and *C*). Fibril growth stopped when one fibril end reached another fibril. This observation was consistent with time-lapse AFM imaging of $A\beta_{1–40}$ (50). During HMW incubation, we observed that nonfibrous particles accumulated more extensively than seen with LMW (Fig. S3*A* and Movie S2). Fibrous objects were also observed (Fig. S3*A*), although they were small in number, and their structural features were consistent with the fibrils seen with LMW (Fig. S3 *B* and *C*). These observations were comparable to electron microscope images and bulk phase assays

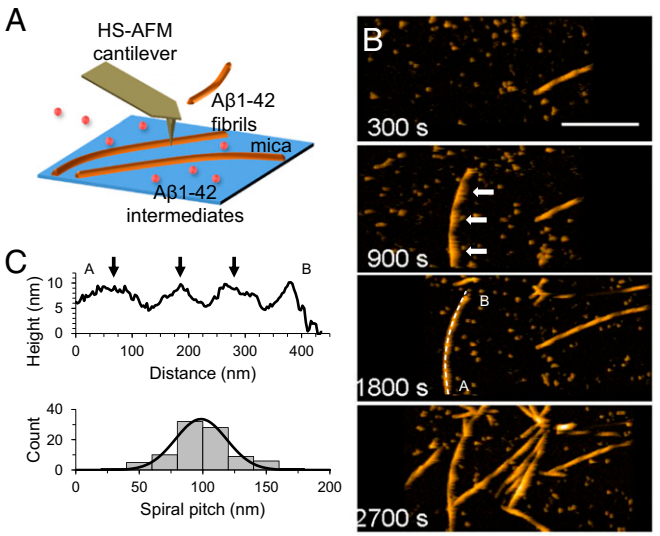

Fig. 1. HS-AFM imaging of LMW $A\beta_{1–42}$. (*A*) Schematic representation of HS-AFM experiments. $A\beta_{1–42}$ was introduced into the HS-AFM chamber. Aggregation was accelerated by addition of 100 mM NaCl. $A\beta_{1–42}$ aggregates float in the chamber, and some of them attached on mica and were visualized. (*B*) HS-AFM images during incubation of LMW. (Scale bar, 300 nm. Z scale, 15 nm.) (*C*) Height profile of the selected dashed line (*A* to *B*) at 1,800 s in *B* (*Top*), and occurrence frequency of the length of the spiral pitch of $A\beta_{1–42}$ fibrils with a normal distribution fit, giving a mean pitch length of 99 ± 20 nm for the fibrils from LMW (*Bottom*). Black arrows correspond to the white arrows in *B* at 900 s.

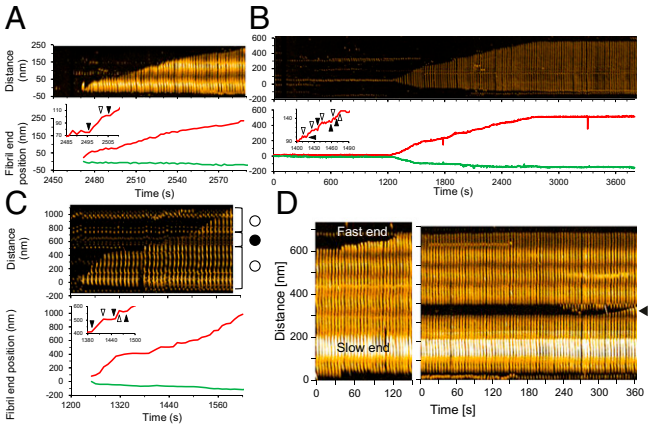

Fig. 2. HS-AFM imaging of fibrils emanating from LMW $A\beta_{1–42}$. (*A–C*) Representative kymographs (*Top*) and time evolution of fast- (red) and slow- (green) growing fibril ends (*Bottom*) of single spiral (*A*), straight (*B*), and hybrid (*C*) types of LMW $A\beta_{1–42}$ fibril elongation. Open and closed circles in *C* indicate the spiral and straight regions in the hybrid fibril. The insets in time evolution: enlarged time courses show representative stepwise growth at fast ends. Starts and ends of individual steps are indicated by closed and open triangles. (*D*) Polarity of $A\beta_{1–42}$ fibril growth. Kymograph of fibril growth before fragmentation (*Left*), indicating polarized elongation in which top and bottom ends of the kymograph indicate fast- and slow-growing ends. Kymograph of fibril growth from exogenous ends of the fibril after fragmentation at the region indicated as a closed triangle (*Right*).

(*Supporting Information* and Fig. S2). We found no significant difference in fibril length between LMW and HMW samples due to the broad distribution of fibril length in the LMW sample (Fig. S3*D*). However, there were significant differences between LMW and HMW samples in the times at which fibril seeds appeared. HMW seeds formed most frequently 20–30 min after the addition of 100 mM NaCl, whereas LMW formed seeds over a much wider time range (Fig. S3 *E* and *F*). We found no significant differences in the nucleation rate or in the fibril seed size between LMW and HMW samples (Fig. S3 *G* and *H*). In addition, some HMW oligomers dissociated during early phases of incubation (*Supporting Information*, Fig. S4, and Movies S3 and S4), after which fibrils formed (Fig. S2*C*). These results suggest that LMW Aβ produced fibril seeds at various time through primary and secondary nucleation events. This suggestion is consistent with previous studies (51, 52). In contrast, HMW Aβ did not directly develop fibril seeds, but first dissociated to LMW Aβ that then formed seeds. Furthermore, these analyses also indicated that the results from HS-AFM observation corresponded to the conventional transmission electron microscope (TEM) images and bulk phase assays. This correspondence was also found in the correlation between the time courses of the total aggregate volume on mica and ThT binding assays (*Supporting Information* and Figs. S2*A* and S3*I*) and supported by observation of fibril growth inhibition in the presence of a natural polyphenolic compound, myricetin (Fig. S5).

Video Imaging of Growth of $A\beta_{1–42}$ Fibrils with Distinct Structures. We next analyzed how individual fibrils formed. We identified three structurally distinct types of fibrils: (*i*) spiral structures of ~100-nm periodicity that varied in height between 5 and 10 nm (Figs. 1 and 2*A* and Movie S5); (*ii*) thin, straight structures of ~5 nm in height (Fig. 2*B* and Movie S6); and (*iii*) hybrid structure in which the spiral and straight structures coexisted (Fig. 2*C* and Movie S7). The growing processes of these fibrils are represented as kymographs and time courses of fibril end positions (Fig. 2 *A–C*). The growth mode is characterized by bidirectional growth, but at different rates at each end (polarization). The polarized bidirectional growth was observed in all of the types of fibrils ("fast and slow ends"

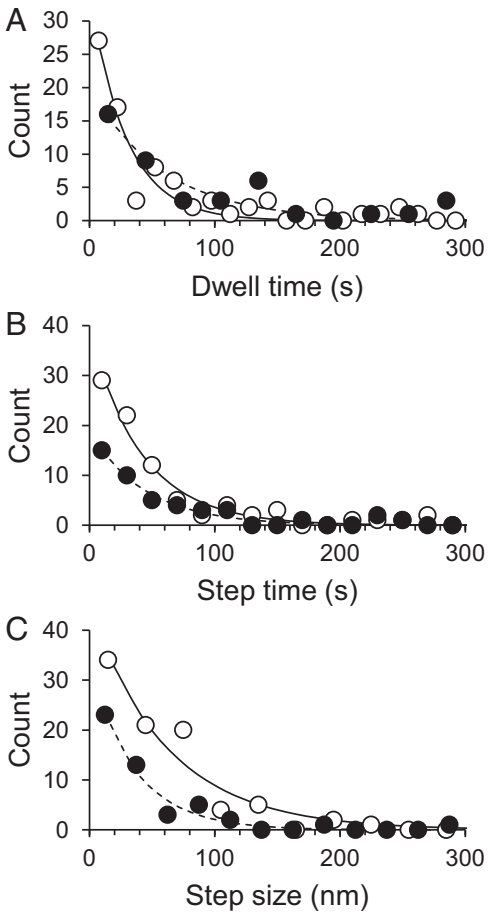

Fig. 3. Statistical analysis of stepwise $A\beta_{1-42}$ fibril growth from LMW incubation. Distributions (circles) of dwell time between steps (*A*), time for a single step (*B*), and single step size (*C*) with exponential fits (lines) giving mean values shown in Table 1, for spiral (open circles with solid lines) and straight (closed circles with dashed lines) fibrils from LMW $A\beta_{1-42}$ incubation.

correspond in Fig. 2 *A–C* to the upper and lower ends in the kymographs and to the red and green lines). Many of the fibrils exhibited stop and go behavior (Fig. 2 *A–C*, *Insets*), as observed for $A\beta_{1-40}$ and other amyloid fibrils (53–56). For example, the fibril growth at the fast end stopped during ~2,488–2,496 s, ~2,502–2,506 s in Fig. 2*A*, ~1,410–1,418 s in Fig. 2*B*, and ~1,420–1,450 s, ~1,460–1,480 s in Fig. 2*C*. We confirmed that the orientation of $A\beta_{1-42}$ fibrils was retained in the interior of the fibrils as follows: (*i*) we broke the fibrils by increasing tapping force, which created new fibril ends; (*ii*) we then observed that at the breakage sites, each of the ends behaved as if it were the original fast or slow end, i.e., the fibril growth rates were consistent with the polarity of the original fibrils (Fig. 2*D*). Fig. 2 *A* and *B* also shows that the structure of growing region was the same as that of the template region. This structural feature in the fibril growth indicates that template structure can determine fibril morphology, which is consistent with a dock-lock mechanism (57). In the hybrid-type fibrils, the structure of the growing region was determined primarily by the template, but sometimes switched to another type (spiral to straight at 1,440 s (145th frame) or straight to spiral at 1,520 s (153rd frame) in Fig. 2*C*).

To quantitatively compare fibril growth kinetics between fibril types, we analyzed stepwise growth of individual fibrils. "Stepwise growth" was considered to comprise two phases: dwell (during which no growth was observed and fibril end position was constant) and step (during which continuous growth was observed and fibril end position increased). Step could further be characterized by step time (each period of continuous growth) and step size (the increase in fibril length occurring during each such period). We observed that the frequency distributions for these three metrics could be described by simply decreasing exponential functions of the type $F = A \cdot e^{-t/\tau}$, where t is time (s^{-1}), A is a constant, and τ is the mean dwell or mean step time (Fig. 3). In the case of step size, t is instantaneous step size and τ is mean step size. The given parameters are shown in Table 1 with the number of analyzed fibrils and steps.

A fast end of spiral fibrils had shorter dwell times and longer step sizes than did those of straight-type fibrils, although their step times are similar. In contrast, the number of steps at a fast end of straight fibrils was larger than that of the spiral fibril. The estimated mean growth length of spiral and straight fibrils was essentially the same (~200 nm). The difference in fibril growth kinetics between LMW and HMW $A\beta_{1-42}$ was described in *Supporting Information*, Fig. S6, and Table S1.

Modulation of Structural Dynamics in $A\beta_{1-42}$ Fibril Growth. To determine whether the switching of fibril structure growing could be modulated by changes in buffer salt, we substituted 100 mM KCl for NaCl. Potassium ions reduce the interactions between proteins and mica surfaces more than do sodium ions (58). Fig. 4*A* shows HS-AFM imaging of $A\beta_{1-42}$ fibrils ~1 h after addition of KCl. Whereas most fibrils grown in NaCl have the spiral structures, the number of hybrid-type fibrils increased in the presence of KCl (Fig. 4*B*). This increase could occur due to (*i*) increase in switching frequency or (*ii*) increase in speed of fibril growth without change in switching frequency. To determine which of these possibilities was true, we analyzed distributions of the full fibril length, the number of partial fibril segments grown with each growth mode (appearance frequency of growth mode), and the length of those segments (length of growth in a single mode). As shown in Fig. 4*C*, the distribution of the full fibril length was not significantly altered by the alteration of buffer salt, which suggests that the fibril growth speed was not affected. Meanwhile, the appearance frequency of spiral and straight modes, respectively, decreased and increased with the replacement of NaCl with KCl (Fig. 4*D*). Consistent with this, the average length of growth in spiral or straight modes decreased or increased, respectively, in the presence of KCl (Fig. 4*E*). This trend was observed in the different preparation of LMW although we found no statistically significant difference in the length of growth in spiral mode in the preparation (Fig. S7). In conclusion, the switching frequency increased in the KCl buffer whereas the fibril growth mode was constrained to the spiral mode in the NaCl buffer.

Table 1. Parameters for stepwise growth kinetics at fast ends of spiral and straight fibrils from LMW

Fibril types	Spiral	Straight
Number of analyzed fibrils	38	10
Number of total analyzed steps*	124	54
Number of steps per one fast end*	3.3	5.4
Dwell time before stepwise growth, s†	29	59
Time required for one step, s†	42	45
Step size, nm†	62	36
Mean growth length, nm‡	204	197

*Steps for 1 h from incubation start, except 15 steps in fibrils from LMW incubation.
†Fitting parameters from Fig. 3.
‡Values obtained from the product of number of steps and step size at fast end.

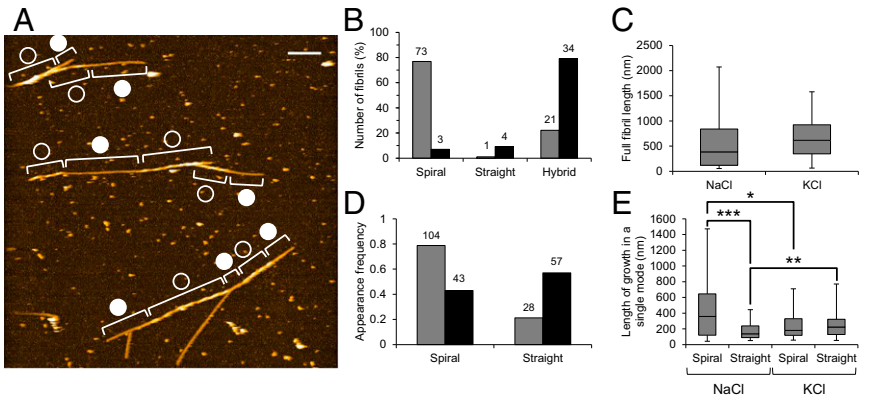

Fig. 4. Electrolyte-dependent kinetics of growth mode switching. (*A*) HS-AFM image of $A\beta_{1-42}$ fibrils from LMW incubation incubated in 10 mM phosphate, pH 7.4, 100 mM KCl for ∼1 h. Open and closed circles indicate the spiral and straight regions in fibrils. (Scale bar, 200 nm. Z scale, 15 nm.) (*B*) Proportion of number of spiral, straight, and hybrid fibril from LMW $A\beta_{1-42}$ incubation in 10 mM phosphate, pH 7.4 containing 100 mM NaCl (gray) or KCl (black). (*C*) Distribution of full lengths of fibrils grown in 10 mM phosphate, pH 7.4, 100 mM NaCl or KCl for ∼1 h. (*D*) Appearance frequencies of spiral and straight growth modes in 10 mM phosphate, pH 7.4 containing 100 mM NaCl (gray) or KCl (black). The numbers of indicated fibrils in the observed area (5.7 × 5.7 μm) are shown on the bars. (*E*) Distribution of lengths of spiral and straight regions in fibrils grown in the presence of 100 mM KCl or NaCl. Boxes extend from the 25th to 75th percentiles. The line in the box signifies the median. The whiskers are drawn from the minimum to 25th percentile value and from 75th percentile value to the maximum. They do not represent SEs. Asterisks indicate statistical significance between the two groups indicated by brackets (*$P < 0.05$, **$P < 0.01$, ***$P < 0.001$, Brunner–Munzel test).

Discussion

We used HS-AFM to monitor the structural dynamics of $A\beta_{1-42}$ fibril formation. This approach allowed us to determine morphological and temporal features of this process for specific $A\beta_{1-42}$ assemblies, including HMW and fibrils. An important finding was a switch in fibril growth mode between "spiral" and "straight" morphomers, even though initial morphologies matched those of the fibril seeds. The frequency of switching was altered by changes in buffer salt. These finding are not consistent with a "dock-lock" model of fibril growth. Switching between morphologies is thought to be extremely rare (essentially nonexistent) when Aβ40 or Aβ42 fibril formation has been studied by TEM. It is possible, therefore, that fibril growth on a mica surface may lead to phenomena that are not observed when fibrils grow freely in solution. However, this finding means that fibril morphology is not absolutely determined by fibril seed structure (nucleus). An implication of this idea is that toxic types of fibrils (seeds) could be converted into nontoxic forms by changes in their cellular or extracellular microenvironments. The converse might also be true.

Our results suggest the following model of $A\beta_{1-42}$ aggregation (Fig. 5). The $A\beta_{1-42}$ aggregation pathway begins with LMW, including monomeric and low-order oligomer states. It then branches into two distinct pathways: (*i*) HMW (off-pathway) and (*ii*) fibril formation via nucleation (on-pathway). Evidence for the first pathway comes from size-exclusion chromatography (SEC) results showing an increase in HMW concentration during LMW incubation (*Supporting Information* and Fig. S4) and from HS-AFM results revealing that some aggregates do not grow into fibrils (Fig. 1*B*). Furthermore, HMW incubation did not sustain fibril growth at early phases (∼30 min of incubation) despite rapid production of LMW $A\beta_{1-42}$ and nucleation rate similar to that of LMW. This difference may be caused by differences in the time when fibril seeds (nuclei) appeared. HMW thus do not appear to be immediate precursors of fibrils, but rather foster fibril formation by dissociation into LMW (*Supporting Information* and Fig. S4). The nuclei and the fibril seeds grow, incorporating LMW $A\beta_{1-42}$ monomers or small assemblies formed by LMW $A\beta_{1-42}$, and the growth rates are different between "fast" and "slow" ends (Fig. 2). This asymmetrical fibril growth is consistent with structural models of Aβ fibrils based on solid-state NMR, in which the two ends of each fibril have different residues available for hydrogen bonding (33). The structure of growing fibrils is typically determined by their seeds [in the context of this discussion, the term "seeds" corresponds to

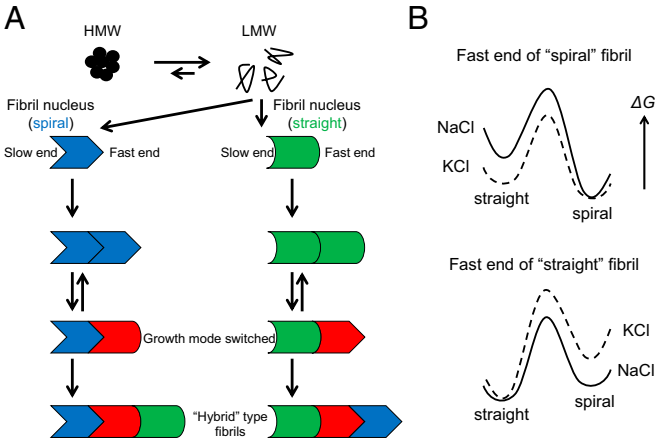

Fig. 5. Models for $A\beta_{1-42}$ aggregation. (*A*) Monomers give rise to at least three assembly pathways for HMW, straight fibrils and spiral fibrils. HMW is not directly linked to fibril formation. HMW dissociates into LMW. The latter two pathways lead to form nuclei, but the nuclei are different in structure between the pathways. The nuclei incorporate LMW $A\beta_{1-42}$ and grow into spiral or straight fibrils with the same type as nuclei in the seed-dependent manner. Switching of fibril growth mode sometimes occurs due to dynamic polymorphism of fibril ends, and thus hybrid fibrils are produced. (*B*) Models of energy profiles for fast ends of spiral- (*Top*) and straight- (*Bottom*) type fibrils. For the end of spiral-type fibril, the energy level of spiral state is much lower than the straight state. Thus, the spiral-type fibril grows in the spiral in accordance with the template-dependent manner, and the switching to straight mode rarely occurs in the NaCl buffer (*Top*, solid line). In the KCl buffer, the energy level of straight state and the activation energy is reduced, which leads to increase in the frequency of switching growth modes (*Top*, dashed line). For the end of straight-type fibril, the energy level of straight is lower than the spiral state, but the difference in the level between the two states may be smaller than that in the spiral fibril end in the NaCl buffer (*Bottom*, solid line). Thus, the straight growth mode is short-lived. In the KCl buffer, the energy level of spiral state and the activation energy is shifted up, which leads to retain the growth with straight mode (*Bottom*, dashed line).

fibril fragments or fibrils themselves. The term "nuclei" refers to the classical thermodynamic structures necessary to initiate a polymerization reaction—in this case by the low-frequency coassociation of LMW Aβ molecules] or nuclei (dock-lock mechanism: the structure of incorporated amyloid proteins is determined by the structure of mother fibril ends). The finding that spiral and straight fibril seeds initially give rise to fibrils of equivalent morphology (Fig. 2 *A* and *B*) supports this idea. $A\beta_{1-42}$ thus produces at least two types of structurally distinct nuclei. The existence of multiple nucleation pathways for one amyloidogenic protein has been reported as described above. Sometimes the growth mode can be switched, which results in the production of "hybrid" fibrils (Fig. 2*C*).

Fibril structural "switching" was an interesting phenomenon that we initially had not expected to observe. It is possible that this occurred due to structural fluctuations at the ends of growing fibrils (59). These spontaneous changes in fibril end structure can be perpetuated by incoming Aβ monomers because these monomers are intrinsically disordered, populate a large volume of conformational space, and thus do not experience substantial energy barriers for binding to fibril ends (60–62). In contrast, the enthalpic and entropic constraints on fibril end structure likely preclude extensive exploration of alternative conformational states, explaining why only two fibril morphologies were observed in our experiment. We note that this fact does not mean other morphologies could not form, only that we did not observe them in the specific experimental system we used. Following our experiments, we learned that dynamic conformational changes in actin filaments also have been observed, supporting the explanation of fibrils switching presented above (63). Additionally, the energy landscape of fibril ends may be altered by the microenvironment (e.g., salt) (Fig. 5*B*).

Goldsbury et al. reported the results of time-lapse AFM imaging of $A\beta_{1-40}$ fibril formation (50). We found similarities and differences in structural dynamics between $A\beta_{1-40}$ and $A\beta_{1-42}$. $A\beta_{1-40}$ protofibrils (PF) and mature fibrils (MF) both exhibited straight and spiral (80–130-nm pitch) morphologies (50), similar to $A\beta_{1-42}$ fibril structures that we observed in the work reported here. MF $A\beta_{1-40}$ formation through lateral interaction between PFs is not a primary assembly pathway (50). We also did not observe lateral interactions among fibrils. In contrast, $A\beta_{1-40}$ and $A\beta_{1-42}$ differed in that formation of spiral and straight $A\beta_{1-40}$ fibrils occurred at different times, whereas both morphologies were observed concurrently in studies of $A\beta_{1-42}$. In addition, our finding of bidirectional switching between spiral and straight growth modes of $A\beta_{1-42}$ has not been reported in any other amyloidogenic protein aggregation.

Materials and Methods

Preparation of Aβ. $A\beta_{1-42}$ peptides were synthesized, purified, and characterized as described previously (49). Briefly, the peptide synthesis was performed on an automated peptide synthesizer (model 433A, Applied Biosystems) using 9-fluorenylmethoxycarbonyl-based methods on preloaded Wang resins. The peptides were purified using reverse-phase high-performance liquid chromatography (HPLC). Quantitative amino acid analysis and mass spectrometry of the yielded peptides confirmed the expected compositions and molecular weights, respectively. The purified peptides were stored as lyophilizates at −20 °C. LMW and HMW Aβ were prepared by SEC (49). To prepare LMW and HMW, 200 μL of a 2 mg/mL peptide solution in dimethyl sulfoxide was sonicated for 1 min using a bath sonicator and then centrifuged for 10 min at 16,000 × *g*. The resulting supernatant was fractionated on a Superdex 75 HR column using 10 mM phosphate buffer, pH 7.4, at a flow rate of 0.5 mL/min. SEC of $A\beta_{1-42}$ reveals an HMW peak at 16–17 min (occurring just after the column void volume) followed by an LMW peak at 28–29 min. The middles of the HMW and LMW peaks were separately collected during 60 s and stored at −80 °C (Fig. S1*A*). The peptide concentration in each preparation was determined by Bradford protein assay. Typically, the concentrations of LMW and HMW were 25 and 10 μM, respectively.

HS-AFM Imaging. Tapping mode HS-AFM (64) was performed at room temperature in liquid with a small cantilever (BL-AC10-DS, Olympus) with a spring constant $k \sim 0.1$ N/m and a resonance frequency $f = 400$–500 kHz. An amorphous carbon tip was grown on the top of each of the cantilevers by electron-beam deposition using a field emission scanning electron microscope (ERA8000-FE, Elionix). The free oscillation amplitude was ∼1.5 nm and the set-point amplitude was 80–90% of the free amplitude. LMW or HMW solutions (2.5 μM peptide concentration in 10 mM phosphate, pH 7.4) were introduced into a sample chamber. $A\beta_{1-42}$ aggregation reactions were accelerated by addition of NaCl (final concentration of 100 mM). For observation of electrolyte effects, the reactions were accelerated by addition of KCl (final concentration of 100 mM) instead of NaCl. For observation of myricetin effects, 2.5 μM $A\beta_{1-42}$ [fibril seeds ($fA\beta_{1-42}$):LMW = 1:19] containing 100 mM NaCl and 10 μM myricetin was introduced into the chamber. The HS-AFM image sequences were processed using ImageJ software (imagej.nih.gov/ij/). The total volume of all of the aggregates in each frame was estimated as the total volume of all of the pixels in the frame except background (mica surface). To assess individual fibril growth, the fibrils were computationally straightened and then their structural features, including length and spiral pitch, were measured and analyzed by ImageJ plugins.

ACKNOWLEDGMENTS. We thank Dr. Noriyuki Kodera, Dr. Hiroki Konno, Prof. Takayuki Uchihashi, and Prof. Toshio Ando (Kanazawa University) for their help in operating HS-AFM, and the anonymous reviewers for comments on earlier version of this paper. This work has been supported by Scientific Research (C) (26461266) (to K.O.) from the Japanese Ministry of Education, Culture, Sports, Science and Technology, Japan; Novartis Foundation for Gerontological Research (K.O.); Takeda Science Foundation (K.O.); NIH Grant AG041295 (to D.B.T.); Grants-in-Aid for Scientific Research (B) (20390242) (to M.Y.) and for Challenging Exploratory Research (15K15336) (to M.Y.) from the Ministry of Education, Culture, Sports, Science, and Technology, Japan; a grant for Amyloidosis Research Committee from the Ministry of Health, Labour and Welfare, Japan (to M.Y.); and a grant for SENSHIN Medical Research Foundation (to M.Y.).

1. LaFerla FM, Green KN, Oddo S (2007) Intracellular amyloid-β in Alzheimer's disease. *Nat Rev Neurosci* 8(7):499–509.
2. Hubin E, van Nuland NA, Broersen K, Pauwels K (2014) Transient dynamics of Aβ contribute to toxicity in Alzheimer's disease. *Cell Mol Life Sci* 71(18):3507–3521.
3. Abelein A, et al. (2014) The hairpin conformation of the amyloid β peptide is an important structural motif along the aggregation pathway. *J Biol Inorg Chem* 19(4-5): 623–634.
4. Weissmann C (2004) The state of the prion. *Nat Rev Microbiol* 2(11):861–871.
5. Aguzzi A, Heikenwalder M, Polymenidou M (2007) Insights into prion strains and neurotoxicity. *Nat Rev Mol Cell Biol* 8(7):552–561.
6. Mead S, Reilly MM (2015) A new prion disease: Relationship with central and peripheral amyloidoses. *Nat Rev Neurol* 11(2):90–97.
7. Prusiner SB (1998) Prions. *Proc Natl Acad Sci USA* 95(23):13363–13383.
8. Goedert M (2001) Alpha-synuclein and neurodegenerative diseases. *Nat Rev Neurosci* 2(7):492–501.
9. Maries E, Dass B, Collier TJ, Kordower JH, Steece-Collier K (2003) The role of α-synuclein in Parkinson's disease: Insights from animal models. *Nat Rev Neurosci* 4(9):727–738.
10. Irwin DJ, Lee VM-Y, Trojanowski JQ (2013) Parkinson's disease dementia: Convergence of α-synuclein, tau and amyloid-β pathologies. *Nat Rev Neurosci* 14(9):626–636.
11. Lee H-J, Bae E-J, Lee S-J (2014) Extracellular α–synuclein-a novel and crucial factor in Lewy body diseases. *Nat Rev Neurol* 10(2):92–98.
12. Cattaneo E, Zuccato C, Tartari M (2005) Normal huntingtin function: An alternative approach to Huntington's disease. *Nat Rev Neurosci* 6(12):919–930.
13. Terry RD, et al. (1991) Physical basis of cognitive alterations in Alzheimer's disease: Synapse loss is the major correlate of cognitive impairment. *Ann Neurol* 30(4): 572–580.
14. Hsia AY, et al. (1999) Plaque-independent disruption of neural circuits in Alzheimer's disease mouse models. *Proc Natl Acad Sci USA* 96(6):3228–3233.
15. Giannakopoulos P, Hof PR, Michel JP, Guimon J, Bouras C (1997) Cerebral cortex pathology in aging and Alzheimer's disease: A quantitative survey of large hospital-based geriatric and psychiatric cohorts. *Brain Res Brain Res Rev* 25(2):217–245.
16. Villemagne VL, et al. (2011) Longitudinal assessment of Aβ and cognition in aging and Alzheimer disease. *Ann Neurol* 69(1):181–192.
17. Aizenstein HJ, et al. (2008) Frequent amyloid deposition without significant cognitive impairment among the elderly. *Arch Neurol* 65(11):1509–1517.
18. Klein WL, Stine WB, Jr, Teplow DB (2004) Small assemblies of unmodified amyloid beta-protein are the proximate neurotoxin in Alzheimer's disease. *Neurobiol Aging* 25(5):569–580.
19. Walsh DM, Selkoe DJ (2007) A beta oligomers - a decade of discovery. *J Neurochem* 101(5):1172–1184.
20. Krafft GA, Klein WL (2010) ADDLs and the signaling web that leads to Alzheimer's disease. *Neuropharmacology* 59(4-5):230–242.

21. Lesné S, et al. (2006) A specific amyloid-beta protein assembly in the brain impairs memory. *Nature* 440(7082):352–357.
22. Noguchi A, et al. (2009) Isolation and characterization of patient-derived, toxic, high mass amyloid beta-protein (Abeta) assembly from Alzheimer disease brains. *J Biol Chem* 284(47):32895–32905.
23. Selkoe DJ (2008) Soluble oligomers of the amyloid beta-protein impair synaptic plasticity and behavior. *Behav Brain Res* 192(1):106–113.
24. Chimon S, et al. (2007) Evidence of fibril-like β-sheet structures in a neurotoxic amyloid intermediate of Alzheimer's β-amyloid. *Nat Struct Mol Biol* 14(12):1157–1164.
25. Deshpande A, Mina E, Glabe C, Busciglio J (2006) Different conformations of amyloid beta induce neurotoxicity by distinct mechanisms in human cortical neurons. *J Neurosci* 26(22):6011–6018.
26. Petkova AT, et al. (2005) Self-propagating, molecular-level polymorphism in Alzheimer's beta-amyloid fibrils. *Science* 307(5707):262–265.
27. Qiang W, Yau W-M, Luo Y, Mattson MP, Tycko R (2012) Antiparallel β-sheet architecture in Iowa-mutant β-amyloid fibrils. *Proc Natl Acad Sci USA* 109(12):4443–4448.
28. Walsh DM, et al. (1999) Amyloid beta-protein fibrillogenesis. Structure and biological activity of protofibrillar intermediates. *J Biol Chem* 274(36):25945–25952.
29. Cameron B, Landreth GE (2010) Inflammation, microglia, and Alzheimer's disease. *Neurobiol Dis* 37(3):503–509.
30. Glass CK, Saijo K, Winner B, Marchetto MC, Gage FH (2010) Mechanisms underlying inflammation in neurodegeneration. *Cell* 140(6):918–934.
31. Sultana R, Perluigi M, Butterfield DA (2009) Oxidatively modified proteins in Alzheimer's disease (AD), mild cognitive impairment and animal models of AD: Role of Abeta in pathogenesis. *Acta Neuropathol* 118(1):131–150.
32. Tõugu V, Tiiman A, Palumaa P (2011) Interactions of Zn(II) and Cu(II) ions with Alzheimer's amyloid-beta peptide. Metal ion binding, contribution to fibrillization and toxicity. *Metallomics* 3(3):250–261.
33. Lu J-X, et al. (2013) Molecular structure of β-amyloid fibrils in Alzheimer's disease brain tissue. *Cell* 154(6):1257–1268.
34. Roychaudhuri R, Yang M, Hoshi MM, Teplow DB (2009) Amyloid β-protein assembly and Alzheimer disease. *J Biol Chem* 284(8):4749–4753.
35. Tycko R, Wickner RB (2013) Molecular structures of amyloid and prion fibrils: Consensus versus controversy. *Acc Chem Res* 46(7):1487–1496.
36. Tycko R (2014) Physical and structural basis for polymorphism in amyloid fibrils. *Protein Sci* 23(11):1528–1539.
37. Meyer-Luehmann M, et al. (2006) Exogenous induction of cerebral beta-amyloidogenesis is governed by agent and host. *Science* 313(5794):1781–1784.
38. Watts JC, et al. (2014) Serial propagation of distinct strains of Aβ prions from Alzheimer's disease patients. *Proc Natl Acad Sci USA* 111(28):10323–10328.
39. Cohen ML, et al. (2015) Rapidly progressive Alzheimer's disease features distinct structures of amyloid-β. *Brain* 138(Pt 4):1009–1022.
40. Ando T, et al. (2001) A high-speed atomic force microscope for studying biological macromolecules. *Proc Natl Acad Sci USA* 98(22):12468–12472.
41. Ando T, Uchihashi T, Kodera N (2013) High-speed AFM and applications to biomolecular systems. *Annu Rev Biophys* 42:393–414.
42. Bitan G, et al. (2003) Amyloid β -protein (Abeta) assembly: Abeta 40 and Abeta 42 oligomerize through distinct pathways. *Proc Natl Acad Sci USA* 100(1):330–335.
43. Walsh DM, Lomakin A, Benedek GB, Condron MM, Teplow DB (1997) Amyloid β-protein fibrillogenesis. Detection of a protofibrillar intermediate. *J Biol Chem* 272(35):22364–22372.
44. Teplow DB (2006) Preparation of amyloid beta-protein for structural and functional studies. *Methods Enzymol* 413(06):20–33.
45. Ono K, Condron MM, Teplow DB (2010) Effects of the English (H6R) and Tottori (D7N) familial Alzheimer disease mutations on amyloid β-protein assembly and toxicity. *J Biol Chem* 285(30):23186–23197.
46. Ono K, Condron MM, Teplow DB (2009) Structure-neurotoxicity relationships of amyloid β-protein oligomers. *Proc Natl Acad Sci USA* 106(35):14745–14750.
47. Harper JD, Lansbury PT, Jr (1997) Models of amyloid seeding in Alzheimer's disease and scrapie: Mechanistic truths and physiological consequences of the time-dependent solubility of amyloid proteins. *Annu Rev Biochem* 66:385–407.
48. Ono K, et al. (2003) Potent anti-amyloidogenic and fibril-destabilizing effects of polyphenols in vitro: Implications for the prevention and therapeutics of Alzheimer's disease. *J Neurochem* 87(1):172–181.
49. Ono K, et al. (2008) Effects of grape seed-derived polyphenols on amyloid β-protein self-assembly and cytotoxicity. *J Biol Chem* 283(47):32176–32187.
50. Goldsbury C, Frey P, Olivieri V, Aebi U, Müller SA (2005) Multiple assembly pathways underlie amyloid-β fibril polymorphisms. *J Mol Biol* 352(2):282–298.
51. Cohen SIA, et al. (2013) Proliferation of amyloid-β42 aggregates occurs through a secondary nucleation mechanism. *Proc Natl Acad Sci USA* 110(24):9758–9763.
52. Meisl G, et al. (2014) Differences in nucleation behavior underlie the contrasting aggregation kinetics of the Aβ40 and Aβ42 peptides. *Proc Natl Acad Sci USA* 111(26): 9384–9389.
53. Qiang W, Kelley K, Tycko R (2013) Polymorph-specific kinetics and thermodynamics of β-amyloid fibril growth. *J Am Chem Soc* 135(18):6860–6871.
54. Kellermayer MSZ, Karsai A, Benke M, Soós K, Penke B (2008) Stepwise dynamics of epitaxially growing single amyloid fibrils. *Proc Natl Acad Sci USA* 105(1):141–144.
55. Ban T, et al. (2004) Direct observation of Abeta amyloid fibril growth and inhibition. *J Mol Biol* 344(3):757–767.
56. Ferkinghoff-Borg J, et al. (2010) Stop-and-go kinetics in amyloid fibrillation. *Phys Rev E Stat Nonlin Soft Matter Phys* 82(1 Pt 1):010901.
57. Esler WP, et al. (2000) Alzheimer's disease amyloid propagation by a template-dependent dock-lock mechanism. *Biochemistry* 39(21):6288–6295.
58. Czajkowsky DM, Shao Z (2003) Inhibition of protein adsorption to muscovite mica by monovalent cations. *J Microsc* 211(Pt 1):1–7.
59. Kusumoto Y, Lomakin A, Teplow DB, Benedek GB (1998) Temperature dependence of amyloid β-protein fibrillization. *Proc Natl Acad Sci USA* 95(21):12277–12282.
60. Zhang S, et al. (2000) The Alzheimer's peptide a β adopts a collapsed coil structure in water. *J Struct Biol* 130(2-3):130–141.
61. Riek R, Güntert P, Döbeli H, Wipf B, Wüthrich K (2001) NMR studies in aqueous solution fail to identify significant conformational differences between the monomeric forms of two Alzheimer peptides with widely different plaque-competence, A β(1-40)(ox) and A β(1-42)(ox). *Eur J Biochem* 268(22):5930–5936.
62. Hou L, et al. (2004) Solution NMR studies of the A β(1-40) and A β(1-42) peptides establish that the Met35 oxidation state affects the mechanism of amyloid formation. *J Am Chem Soc* 126(7):1992–2005.
63. Kozuka J, Yokota H, Arai Y, Ishii Y, Yanagida T (2006) Dynamic polymorphism of single actin molecules in the actin filament. *Nat Chem Biol* 2(2):83–86.
64. Uchihashi T, Kodera N, Ando T (2012) Guide to video recording of structure dynamics and dynamic processes of proteins by high-speed atomic force microscopy. *Nat Protoc* 7(6):1193–1206.
65. LeVine H, 3rd (1993) Thioflavine T interaction with synthetic Alzheimer's disease β-amyloid peptides: Detection of amyloid aggregation in solution. *Protein Sci* 2(3): 404–410.
66. Potapov A, Yau W-M, Ghirlando R, Thurber KR, Tycko R (2015) Successive stages of amyloid-β self-assembly characterized by solid-state nuclear magnetic resonance with dynamic nuclear polarization. *J Am Chem Soc* 137(25):8294–8307.